

## Article

# Hydroxyapatite-Barium Titanate Biocoatings Using Room Temperature Coblasing

Inês J. G. Dias <sup>1</sup>, A. Sofia Pádua <sup>1,2</sup> , Eduardo A. Pires <sup>3</sup>, João P. M. R. Borges <sup>1,\*</sup> , Jorge C. Silva <sup>2,\*</sup>   
and M. Carmo Lança <sup>1,\*</sup> 

<sup>1</sup> CENIMAT | i3N, Department of Materials Science, School of Science and Technology, NOVA University Lisbon, 2829-516 Caparica, Portugal

<sup>2</sup> CENIMAT | i3N, Department of Physics, School of Science and Technology, NOVA University Lisbon, 2829-516 Caparica, Portugal

<sup>3</sup> Bioceramed, R. José Gomes Ferreira n°1 Arm. D, 2660-360 São Julião do Tojal, Portugal

\* Correspondence: jpb@fct.unl.pt (J.P.M.R.B.); jcs@fct.unl.pt (J.C.S.); mcl@fct.unl.pt (M.C.L.)

**Abstract:** The use of orthopaedic and dental implants is expanding as a consequence of an ageing population and also due to illness or trauma in younger age groups. The implant must be bio-compatible, bioactive and interact favourably with the recipient's bone, as rapid osseointegration is key to success. In this work, Ti-6Al-4V plates were coated using the CoBlast™ technique, with hydroxyapatite (HAp) and HAp/BaTiO<sub>3</sub> (barium titanate, BT) non-piezoelectric cubic nanopowders (HAp/cBT) and piezoelectric tetragonal micropowders (HAp/tBT). The addition of BT, a piezoelectric ceramic, is a strategy to accelerate osseointegration by using surface electric charges as cues for cells. For comparison with commercial coatings, plates were coated with HAp using the plasma spray technique. Using XRD and FTIR, both plasma spray and CoBlast™ coatings showed crystalline HAp and no presence of by-products. However, the XRD of the plasma-sprayed coatings revealed the presence of amorphous HAp. The average surface roughness was close to the coatings' thickness (≈5 μm for CoBlast™ and ≈13 μm for plasma spray). Cytotoxicity assays proved that the coatings are biocompatible. Therefore, it can be concluded that for HAp-based coatings, CoBlast™ is a viable alternative to plasma spray, with the advantage of facilitating room temperature addition of other ceramics, like piezoelectric BaTiO<sub>3</sub>.

**Keywords:** CoBlast™; plasma spray; hydroxyapatite; barium titanate



**Citation:** Dias, I.J.G.; Pádua, A.S.; Pires, E.A.; Borges, J.P.M.R.; Silva, J.C.; Lança, M.C. Hydroxyapatite-Barium Titanate Biocoatings Using Room Temperature Coblasing. *Crystals* **2023**, *13*, 579. <https://doi.org/10.3390/cryst13040579>

Academic Editors: Madalina Simona Baltatu, Petrica Vizureanu and Andrei Victor Sandu

Received: 4 February 2023

Revised: 8 March 2023

Accepted: 11 March 2023

Published: 28 March 2023



**Copyright:** © 2023 by the authors. Licensee MDPI, Basel, Switzerland. This article is an open access article distributed under the terms and conditions of the Creative Commons Attribution (CC BY) license (<https://creativecommons.org/licenses/by/4.0/>).

## 1. Introduction

The use of orthopaedic and dental implants has expanded in recent decades due to the acceleration of an ageing population and the practice of increasingly dangerous sports and orthopaedic disorders, which affect millions of patients [1,2]. Thus, there is an urgent and immediate need to develop bone treatment alternatives that improve the performance and durability of implants to increase the patient's life quality and reduce problems caused by damaged or diseased bone tissue. Orthopaedics market sales in 2022 were estimated at EUR 51,000 million worldwide, with a growth rate of 3.4% compared to 2021 and close to the pre-COVID average growth rate [3]. Furthermore, the world market for orthopaedic implants is expected to be valued at EUR 70,000 million by 2030 according to Quintille Insights-HealthCare [4].

Due to the complexity of the musculoskeletal system, which performs structural, protective and mechanical functions in the human body, extensive research on bone healing is needed to develop functional replacements for diseased/malfunctioning joints or bone-anchored elements [5]. The emergence of modern biology has provided new insights into the biological mechanisms responsible for bone healing, which currently facilitates the development of artificial implants [5–7]. The new generation of implants uses materials that, in addition to having good mechanical properties, also provoke a natural response

from the organism as if the graft were bone, maintaining the normal activity of osteoblasts and osteoclasts [8,9].

One of these materials is hydroxyapatite (HAp) due to its similarity in composition with the inorganic phase of human bone and teeth and capacity to form a direct bond with the surrounding bone tissue [10–12]. However, despite the biological benefits of using HAp, in bulk this material presents the typical behaviour of a ceramic: it has a brittle behaviour and has both low tensile strength and impact resistance [13,14]. Therefore, HAp is often used as a coating material in bone- and teeth-load-bearing implants.

In an effort to combine the mechanical properties and corrosion resistance of metals and metal alloys with the biological properties of HAp, several coating techniques have been developed, such as sol-gel, ion-beam, electrophoretic, high-velocity oxy-fuel spray (HVOF,) plasma spray (PS) and CoBlast<sup>TM</sup> (CB) [15,16]. PS is the main industrial deposition process since the resulting coating has a micrometric surface roughness with variable coating thickness allied to a high deposition rate, good biocorrosion resistance and substrate fatigue resistance [17–19]. A major issue with the plasma-sprayed HAp coatings is the thermal modification of the powder's crystalline phases during the deposition process. These modifications result in multi-phase coatings: PS HAp coatings consist not only of crystalline HA but also of amorphous HAp, beta-tricalcium phosphate ( $\beta$ -TCP), alpha-tricalcium phosphate ( $\alpha$ -TCP, results from  $\beta$ -TCP above 1600 K) and tetra-calcium phosphate (TTCP) [18–20]. The decreased crystallinity results in increased solubility of the coating, which, in turn, may result in separation of the coating from the device and possibly unsatisfactory in vivo bone fixation [20–22].

CB is a room temperature and atmospheric pressure blast coating technique that is used for the deposition of thin coatings [23]. The low temperature process avoids phase changes and the resulting increase in solubility levels found in the PS process [15,24]. Furthermore, Barry et al. studied the bioactivity of HAp coatings obtained by CB and concluded that these coatings undergo two stages of recrystallisation. The first stage is homogenous nucleation and, after 7 days of immersion in a simulated body fluid, a heterogeneous nucleation mechanism. The initial stage allows a calcium phosphate layer to grow without significantly altering the morphology, resulting in an increase in the overall coating thickness and roughness. The next stage reduced coating roughness, without altering coating thickness [25].

The in vitro osteoconduction and in vivo osseointegration was analysed by Tan et al. [26]. Their results show that PS and CB HAp coatings have comparable bioactivity at the cellular and tissue levels. Moreover, CB HAp presented greater tolerance to impactions allowing it to be used in more stress-prone surgical applications [26].

Bone piezoelectricity appears to be mainly due to the aligned collagen fibres, the main organic component of bone, and the role of hydroxyapatite is still under debate [27]. The role of mechanical loading on bone remodelling was first mentioned by Wolf in 1892 (Wolff's law [28]) and lately it was associated with the direct piezoelectric effect, i.e., converting a mechanical stimulus into an electric response [29]. The electric signals are a cue for bone cells: bone remodelling is a continuous equilibrium process of formation by osteoblasts and dissolution by osteoclasts. In vivo studies have shown that electrically charged surfaces enhance bone tissue regeneration [30]. Since barium titanate is a well-known piezoelectric biocompatible ceramic, composites of HAp/BT have been studied to match the piezoelectric character of bone with remodelling responding to electrical signals generated by mechanical stress [27]. Only recently was plasma spray deposition successfully used for coatings of HAp and barium titanate. The results showed that none of the materials were modified by the coating process [31,32].

In this work, a comparative study was conducted using samples of uncoated Ti-6Al-4V plates, samples coated with HAp by CoBlast<sup>TM</sup> (CB HAp), Plasma Spray (PS HAp), 80%/20% (m/m) HAp/BaTiO<sub>3</sub> using non-piezoelectric cubic nanopowders (HAp/cBT) and piezoelectric tetragonal micropowders (HAp/tBT) by CoBlast<sup>TM</sup>. Materials were characterised to find if any phase changes occurred and if by-products of the deposition

appeared. Surface roughness was evaluated, and cytotoxicity assays performed. The properties studied allowed to determine if CB is a viable alternative to PS.

## 2. Materials and Methods

### 2.1. Materials

For the development of this work, the substrate used was titanium alloy (Ti-6Al-4V) Grade 5 ASTM B265 cut into 15 mm × 15 mm × 2 mm plates using a water jet cutter (Jacquet, Ovar, Portugal), commercial hydroxyapatite micropowders (Altakitin, Aveiro, Portugal), barium titanate (Sigma-Aldrich, Saint Louis, MO, USA) non-piezoelectric cubic nanopowders (average particle size  $\leq 100$  nm) and piezoelectric tetragonal micropowders (average particle size  $\leq 3$   $\mu\text{m}$ ), and abrasive corundum F20 for samples produced by Plasma Spray and abrasive corundum F120 for samples produced by CB (Blasqem, Maia, Portugal).

For the cell tests, the medium used was DMEM (Dulbecco's Modified Eagle's Medium, Sigma-Aldrich #D5030) supplemented with 1.0 g/L D-glucose (Gibco, ThermoFischer Sci., Waltham, MA, USA #15023-021), 3.7 g/L sodium bicarbonate (Sigma-Aldrich, #S5761), 1% GlutaMAX™ (L-alanyl-L-glutamine dipeptide, Gibco, #35050-038), 1% sodium pyruvate (Gibco, #11360039), penicillin (100 U/mL), streptomycin (100  $\mu\text{g}/\text{mL}$ ) (Gibco, #15140122), and 10% FBS (Fetal Bovine Serum, Gibco, #10270106).

### 2.2. CB and PS

All substrates underwent pre-deposition processes including mechanical polishing of substrate edges and vertices, cleaning in an ultrasonic bath (VWR Ultrasonic Cleaner USC-TH, Radnor, PA, USA) with anti-corrosive detergent (Surfaclean 995, Kiesow Oberflächenchemie, Detmold, Germany) at 50 °C for 15 min, washing under running water and immersion in methanol for 2 min. Then, for samples used for the plasma spraying, a grit blasting with abrasive F20 was necessary to increase surface roughness.

Atmospheric Plasma Spray (APS) was the technique used to deposit the HAp coatings using micrometric HAp powders (APS system Sulzer Metco, Winterthur, Switzerland). The CB coating processes were carried out at Bioceramed using the setup presented in Figure 1. The CB coatings were deposited in a system already reported [15], [26] from EnBIO, Cork, Ireland. Briefly, the 1:1 samples of HAp, average particle size  $\approx 35$   $\mu\text{m}$ , and corundum ( $\text{Al}_2\text{O}_3$ ), abrasive F120, average particle size  $\approx 106$   $\mu\text{m}$ , were mixed (Sulzer Metco Single 10-C Powder Feeder) for 5 min at 60 rpm and 6 bar, and then supplied by a powder feeder to the nozzle. This nozzle blasts the mixture onto metallic substrates.

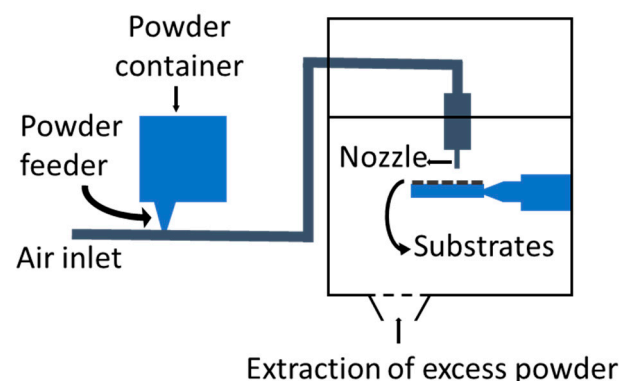


**Figure 1.** CB experimental setup. Inspired by [33].

The essential deposition parameters including particle size, nozzle angle and height, powder feeder pressure and deposition direction are summarised in Table 1. At the end of the process, all samples underwent post deposition cleaning using filtered dry air to remove non-adhered particles.

**Table 1.** Deposition Parameters used in CB coating process.

| Deposition Parameters               |             |
|-------------------------------------|-------------|
| HAp particle size ( $\mu\text{m}$ ) | 35          |
| Nozzle angle ( $^\circ$ )           | 90 $^\circ$ |
| Height (mm)                         | 40          |
| Feeder pressure (bar)               | 4           |
| Forward speed (mm/s)                | 13          |

A summary of the coatings under study is presented in Table 2, including deposition method and composition.

**Table 2.** Coating method of deposition and composition.

| Deposition | Sample  | Materials (m/m%) |                                |     | tBT |
|------------|---------|------------------|--------------------------------|-----|-----|
|            |         | HAp              | Al <sub>2</sub> O <sub>3</sub> | cBT |     |
| PS         | Hap     | 100              |                                |     |     |
| CB         | Hap     | 50               | 50                             |     |     |
|            | HAp/cBT | 40               | 50                             | 10  |     |
|            | HAp/tBT | 40               | 50                             |     | 10  |

### 2.3. Characterisation

The X-ray diffraction (XRD) technique was used to determine coating composition and their crystal phases in the coatings produced. These analyses were performed using an X'Pert PRO PANALytical (Malvern, UK) X-ray powder diffractometer (Cu K-alpha radiation) operating at 45 kV and 40 mA over a 2 $\theta$  range from 10 $^\circ$  to 90 $^\circ$  and step 0.033 $^\circ$ .

Fourier Transform Infrared (FTIR) spectroscopy was performed on the different materials using a Thermo Nicolet 6700 spectrometer (ThermoFischer, Waltham, MA, USA) in a wave number range from 5000–500 cm<sup>-1</sup>.

The surface morphology of the coatings was examined in a field emission SEM (Auriga, from Zeiss, Oberkochen, Germany). The samples were mounted on aluminium platforms and then sputter-coated with a 60% gold–40% palladium conductive layer (Q3000T D Quorum, Laughton, UK, sputter coater). The images were taken at an accelerating voltage of 15 kV and several magnifications.

The surface roughness and topography of the coatings produced were analysed using a confocal microscope (Zeiss LSM 700) with a laser of 405 nm and a z-step of 2.12  $\mu\text{m}$ . Subsequently, image analysis was performed using ZEN 2.1 software (Zeiss). A low-pass filter ( $W$ ) was applied to each image to smooth and enhance image details and minimise noise effects, without changing the average grey scale of the image (representing the value of roughness). Confocal microscopy can also measure the average roughness of a surface area ( $W_{Sq}$ ) and Gaussian distribution statistical parameters, such as curve asymmetry ( $W_{Ssk}$ ) and flattening of the data ( $W_{Ssu}$ ).

For coating thickness measurement, an Elcometer 456 thickness gauge (Manchester, UK) was used for measurements on metallic substrates.

The cytotoxicity tests were performed using the Vero cell line and the extract method according to the ISO 10993-5 standard. Samples were sterilised with ethanol for 5 min and then left to dry at room temperature. The extracts were prepared by immersing each coating with an exposed area of 0.5 cm<sup>2</sup> for each ml of culture medium for 48 h at 37  $^\circ\text{C}$  and in a controlled 5% CO<sub>2</sub> atm. Cells were seeded at a density of 20 k cells/cm<sup>2</sup> in a 96-well microplate and incubated for 24 h. Then, the medium was exchanged for the extracts and two dilutions ( $C_{0/2}$  and  $C_{0/4}$ ) were made, each with five replicates. For the resazurin test, a negative control (cells cultured in a standard, non-cytotoxic environment) and a positive control (cells in a cytotoxic environment, created through the addition of 10% of DMSO, a cytotoxic agent, to normal culture medium) were set. The extracts and controls were incubated for 48 h and afterwards the media were replaced by a 90% culture medium and

10% resazurin solution and incubated for 3 h. Cell viability was evaluated by measuring the absorbance of the medium at 570 nm and 600 nm using a microplate reader (Biotek ELx 800 UV, Winooski, VT, USA). Cell viability was calculated as the percentage of the negative control, given by Equation (1):

$$\text{Cell Viability (\%)} = \frac{\text{OD}_{570-600} \text{ Sample}}{\text{OD}_{570-600} \text{ Negative Control}} \times 100 \quad (1)$$

### 3. Results

#### 3.1. XRD

Figure 2 displays the X-ray diffractograms of the different coatings studied. Crystalline phases were identified using JCPDS-ICCD Powder Diffraction File (PDF) datasheets: #09-0432 hexagonal HAp; #00-005-0626 cubic and #01-084-9618 tetragonal BaTiO<sub>3</sub>; #00-046-1212 rhombohedral Al<sub>2</sub>O<sub>3</sub> and #00-044-1294  $\alpha$ -hexagonal closed-packed-HCP and #00-009-0098  $\beta$ -body-centred cubic-BCC titanium (since Ti-6Al-4V is defined as  $\alpha$ - $\beta$  titanium alloy).

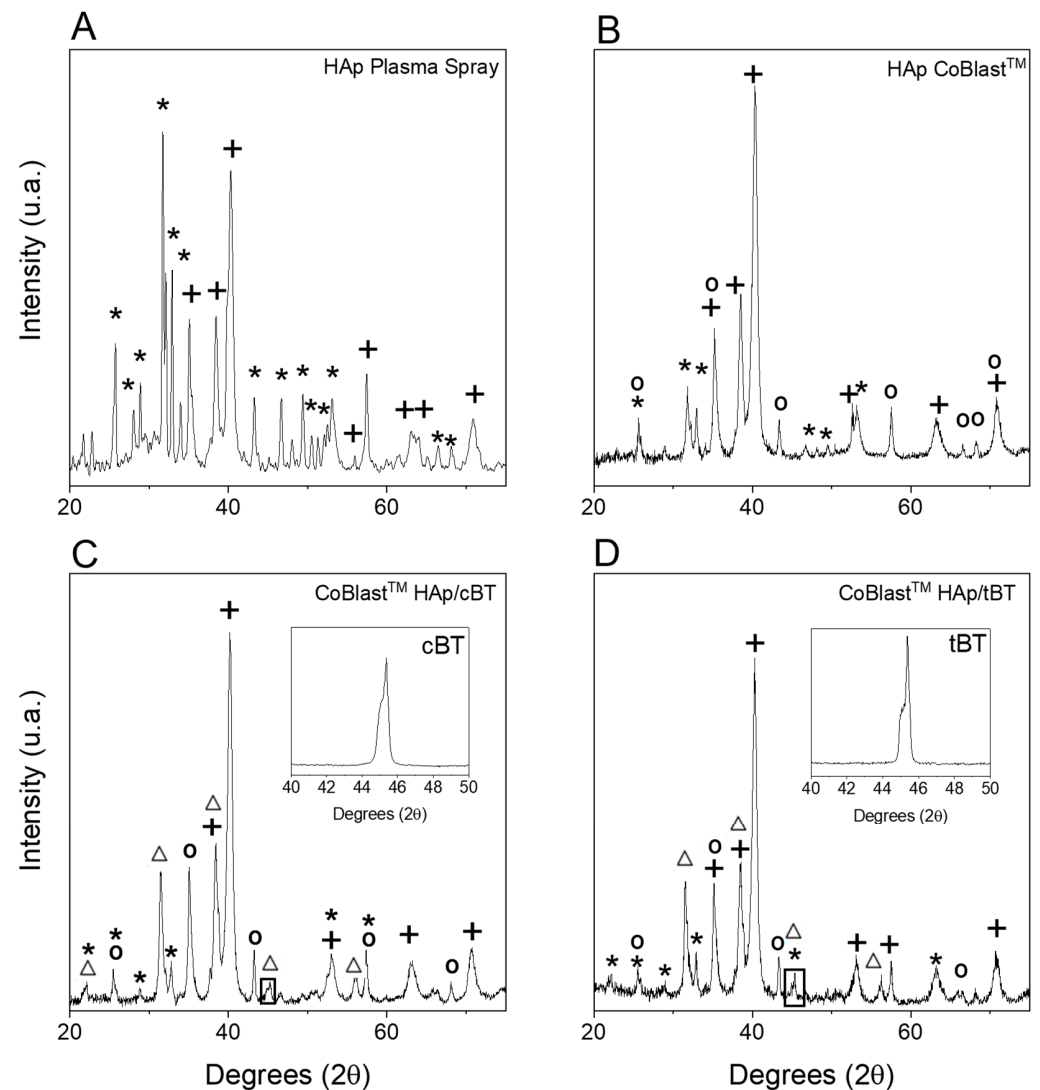


**Figure 2.** XRD analysis of the different coatings produced: HAp by plasma spray (A) and by CoBlast™ of HAp (B), 80%/20% HAp/BaTiO<sub>3</sub> cubic nanopowders (C), 80%/20% of HAp/BaTiO<sub>3</sub> tetragonal micropowders (D). +—Ti-6Al-4V; \*—HAp; o—Al<sub>2</sub>O<sub>3</sub>; Δ—BT.

The diffractograms of the hydroxyapatite coatings on the titanium alloy, by PS and CB, presents the crystalline peaks of hexagonal P6<sub>3/m</sub> HAp [34] and of the metallic substrate

( $\alpha$ -Ti and  $\beta$ -Ti) [35], as can be observed in Figure 2A (PS) and B (CB). Previous studies have shown that the Ti-6Al-4V is known to have  $\alpha$ -Ti (HCP) and  $\beta$ -Ti (BCC) phases present at room temperature [35–39]. The Ti alloy peaks are among the more intense, as expected, since we have a thin film deposited on a metallic plate 2 mm thick. The films' thickness, measured with the thickness gauge, are  $(13 \pm 6)$   $\mu\text{m}$  for PS and  $\approx 5$   $\mu\text{m}$  for CB. Moreover, the CB coating presents alumina (abrasive) peaks (Figure 2B–D) used to remove a surface layer from the Ti alloy to increase surface roughness, enhancing adhesion of the film [40] and improving in vivo osteointegration [41].

Present in Figure 2C,D, are the diffractograms of the composite coatings of 80/20 ( $w/w\%$ ) HAp/BT of cubic nanopowders (HAp/cBT) and tetragonal micropowders (HAp/tBT), respectively. BT identifying peaks are seen, and in Figure 2D, the inset taken at approximately  $45^\circ$  shows the typical double peak for the tetragonal phase as expected for tBT. For cBT, the double peak separation (see Figure 2C) is much less pronounced, which points to a much higher content of the cubic phase compared with the tetragonal one.

For PS HAp (Figure 2A), there appears to be a hump around  $30^\circ$ , which points to the presence of an amorphous phase, as expected for HAp when using the plasma spray technique [42,43]. The absence of further newly formed phases reveals that there are no phase changes, apart from the one already mentioned, and no by-products resulting from the coating processes.

From the diffractograms, it is possible to estimate the size of the HAp crystallites for the two types of coatings under study (PS and CB). For this, we used the Scherrer equation (Equation (2)) where  $L$  is the crystallite size to be determined,  $\lambda$  is the wavelength of X-ray radiation,  $b$  is the broadening of the peak (rad),  $\theta$  is the diffraction angle at peak maximum and  $K$  is a constant [44].

$$L = \frac{K\lambda}{b \cos \theta} \quad (2)$$

The peaks were fitted by the least-squares method and used to estimate  $b$  (full width at half maximum FWHM). The wavelength for Cu- $K\alpha$  radiation is  $\lambda = 1.5418 \times 10^{-10}$  m and the chosen value of the constant was  $K = 0.9$ . For HAp, the more intense peak (211) was chosen. Even if this peak is not an isolated peak for hydroxyapatite, in the patterns obtained, it is not superimposed with the more intense peaks of the other materials present. The  $2\theta$  values of the maxima found for the (211) plane were  $31.73^\circ$  for PS and  $31.83^\circ$  for CB. The calculated average crystallite sizes for the PS and CB HAp coatings were approximately 41.6 nm and 28.0 nm, respectively. For the FWHM, uncertainty is usually not estimated because the values obtained for the uncertainty are a rough underestimation of the true error [45]. The higher value obtained for PS HAp may be due to the high temperatures needed in this technique, causing an increase in size by coalescence of the crystallites. The same does not occur in CB deposition since it is performed at room temperature.

Additionally, the average crystallite diameter was determined for HAp and BaTiO<sub>3</sub> in both types of coatings (HAp/cBT and HAp/tBT). For barium titanate, the peak chosen (110) is well-differentiated in the pattern and is also the most intense (Figure 2C,D). The same procedure used for PS and CB HAp XRD results was followed. The values for the  $2\theta$  estimated for HAp were  $31.79^\circ$  for both HAp/cBT and HAp/tBT, whereas for BT were  $31.43^\circ$  (HAp/cBT) and  $31.49^\circ$  (HAp/tBT). For the CB coating with cubic BT, the calculated average crystallite sizes were approximately 21.0 nm for HAp micropowders and 17.1 nm for BT nanopowders. For the coating with tetragonal BT, the sizes determined were 13.0 nm for HAp and 18.4 nm for BT nanopowders. The hydroxyapatite crystallite sizes are much smaller than the ones found for CB HAp coatings. A summary of these results is presented in Table 3.

**Table 3.** XRD results for crystallite size and lattice parameters.

| Material | Sample  | Crystallite Size |               |          | Lattice Parameters       |         |         |
|----------|---------|------------------|---------------|----------|--------------------------|---------|---------|
|          |         | (hkl)            | $2\theta$ (°) | $L$ (nm) | Sample                   | $a$ (Å) | $c$ (Å) |
| HAp      | PS HAp  | (211)            | 31.73         | 41.6     | PS HAp                   | 9.440   | 6.921   |
|          | CB HAp  |                  | 31.83         | 28.0     | CB HAp                   | 9.720   | 6.947   |
|          | HAp/cBT |                  | 31.79         | 21.0     | JCPDS/ICDD #09–0432      | 9.418   | 6.884   |
|          | HAp/tBT |                  | 31.79         | 13.0     |                          |         |         |
| cBT      | HAp/cBT | (110)            | 31.43         | 17.1     | Rietveld refinement [43] | 9.399   | 6.916   |
| tBT      | HAp/tBT |                  | 31.49         | 18.4     |                          |         |         |

Lattice parameters  $a$  and  $c$  for hexagonal HAp coating by PS and CB were calculated using Bragg's law applied to diffraction data peaks: (002) to obtain  $c$  and (300) for  $a$ . Interplanar spacing was obtained directly from Bragg's law and  $2\theta$  positions for (300) and (002), respectively. Finally, from Equation (3), for the interplanar spacing in a hexagonal lattice, the parameters were estimated ( $d = d_{hkl}$ ):

$$\frac{1}{d^2} = \frac{4}{3} \left( \frac{h^2 + hk + k^2}{a^2} \right) + \frac{l^2}{c^2} \quad (3)$$

Estimated values for PS coating are  $a = 9.440$  Å and  $c = 6.921$  Å and for CB coating  $a = 9.720$  Å and  $c = 6.947$  Å. Calculated values for both coatings are higher than the standard tabulated values for hexagonal HAp:  $a = 9.418$  Å and  $c = 6.884$  Å (JCPDS #09–0432), since a rearrangement of the atoms in the lattice is expected. For PS coatings with HAp, the values found in the literature using Rietveld refinement have an identical behaviour (for instance Shamray [43] obtained average values of  $a = 9.399$  Å and  $c = 6.916$  Å, while another study also found similar results [46]). In the HAp unit cell, there are two  $\text{Ca}_5(\text{PO}_4)_3$  clusters and the HAp structure can be seen as a double layer of two (001) clusters. After PS, interaction between the clusters in the same layer increases, while it decreases between layers, resulting in lattice parameters increasing [43]. Regarding CB HAp coatings, as far as the authors know, absent from the literature are values of the lattice parameters after coblasting. From the results presented above, there is a much higher distortion of the unit cell of HAp compared to PS deposition, as stated above for crystallite size, which could be caused by the impact stress and the high amount of corundum in the blasted mixture during CB deposition.

### 3.2. FTIR

To identify the presence of functional groups characteristic of the different materials used in the coatings on the Ti-6Al-4V samples, Fourier transform infrared analysis was performed.

The bands were assigned to functional groups according to the data summarized in Table 4. The FTIR spectra of PS HAp coating, in Figure 3A, shows the main bands of HAp. They are the broad peaks centred between  $1115 \text{ cm}^{-1}$  and  $1020 \text{ cm}^{-1}$ , in the range from  $925 \text{ cm}^{-1}$  to  $960 \text{ cm}^{-1}$  and at  $580 \text{ cm}^{-1}$ . The first two bands correspond to P–O vibrating bonds of the phosphate groups in the asymmetric stretching mode, the third to a symmetric stretching mode of the same group and the last two to the asymmetric bending modes of  $\text{PO}_4^{3-}$  [47–49]. Additionally visible is the band for carbonate bonds ( $\text{CO}_3^{2-}$ ) located at  $870 \text{ cm}^{-1}$ , a result of the asymmetric bending mode of  $\text{CO}_3^{2-}$  [48,50]. This band is related to type B carbonated hydroxyapatite, corresponding to the substitution of phosphate groups by carbonate [50].

Concerning the spectra of CB HAp (Figure 3B), the same bands characteristic of HAp are present, though they are seen as less intense due to the presence of the abrasive

(50/50 HAp/Al<sub>2</sub>O<sub>3</sub> (*w/w*%)). In plasma spray, the coating is 100% HAp. Furthermore, the carbonate group band is not detected.

**Table 4.** Assignment of FTIR spectra of HAp by PS and HAp, HAp/cBT and HAp/tBT by CB coatings presented in Figure 3 [47–52].

| Samples            | IR Absorption Bands (cm <sup>-1</sup> ) | Description   |
|--------------------|---|---|
| HAp<br>(PS and CB) | 1115                                    | $\nu_{3'}(\text{PO}_4^{3-})$ asymmetric stretching mode |
|                    | 1020                                    | $\nu_3(\text{PO}_4^{3-})$ asymmetric stretching mode    |
|                    | 925–960                                 | $\nu_1(\text{PO}_4^{3-})$ symmetric stretching mode     |
|                    | 870                                     | $\nu_2(\text{CO}_3^{2-})$ asymmetric bending mode       |
|                    | 580                                     | $\nu_4(\text{PO}_4^{3-})$ asymmetric bending mode       |
| HAp/BT             | 2400                                    | O=C=O from BaCO <sub>3</sub>                            |
|                    | 1100                                    | $\nu_{3'}(\text{PO}_4^{3-})$ asymmetric stretching mode |
|                    | 1000                                    | $\nu_3(\text{PO}_4^{3-})$ asymmetric stretching mode    |
|                    | 960                                     | $\nu_1(\text{PO}_4^{3-})$ symmetric stretching mode     |
|                    | 540                                     | $\nu(\text{BaTiO}_3)$ stretching mode                   |
|                    | 530                                     | $\nu(\text{OH}^-)$ stretching mode                      |

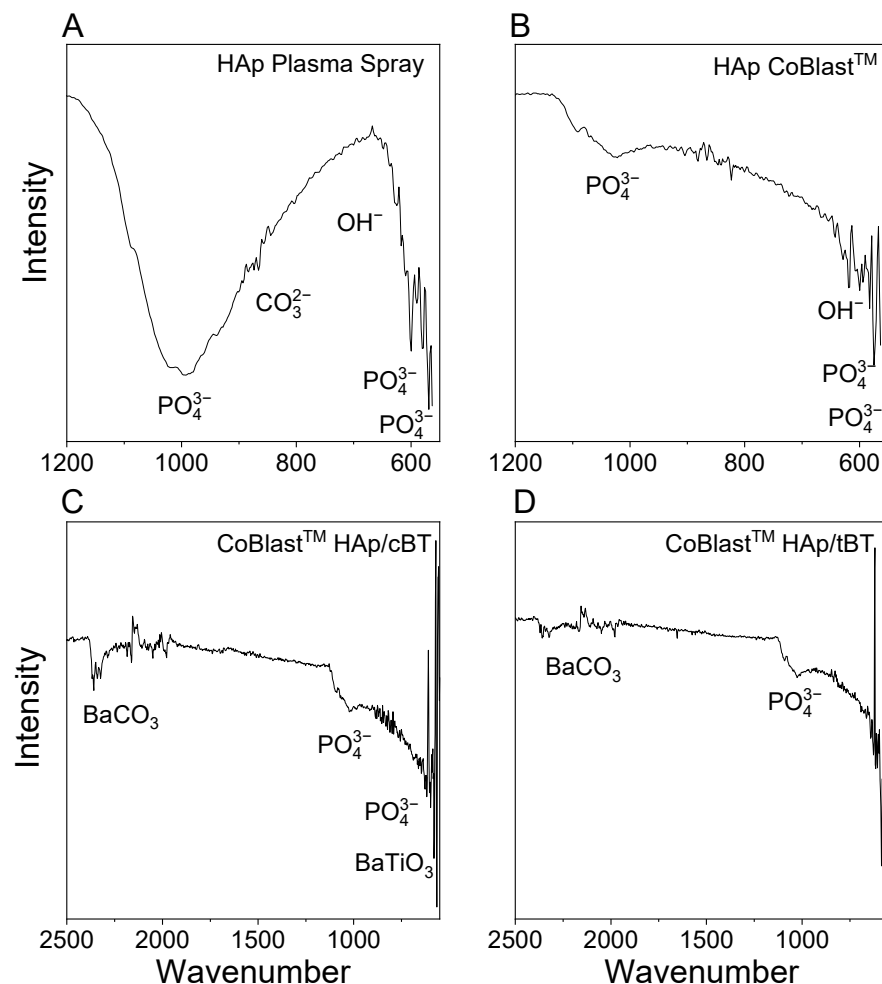


**Figure 3.** FTIR spectra of HAp by Plasma Spray coating (A) and coatings by CoBlast™ with HAp (B), 80%/20% of HAp/BaTiO<sub>3</sub> cubic structure (C), 80%/20% of HAp/BaTiO<sub>3</sub> tetragonal structure (D).

In Figure 3C,D are the CoBlast CB HAp/cBT and HAp/tBT FTIR spectra, respectively. Both present typical bands of HAp and BaTiO<sub>3</sub>. Once again, for HAp, a broad band at approximately 1000 cm<sup>-1</sup> is visible that corresponds to P–O bond vibrations of the PO<sub>4</sub><sup>3-</sup>

group, with the highest intensity vibration peak of this group appearing in the region between  $960\text{ cm}^{-1}$  (symmetric stretching) and  $1100\text{ cm}^{-1}$  (asymmetric stretching mode). Furthermore, the  $\text{OH}^-$  groups stretching mode is observed at  $530\text{ cm}^{-1}$ . Additionally visible are the Ti–O stretching mode absorption bands around  $540\text{ cm}^{-1}$  and  $2400\text{ cm}^{-1}$ , which are the molecular fingerprints of the crystalline  $\text{BaTiO}_3$  for both cubic and tetragonal phases [51,52]. The peaks at approximately  $2400\text{ cm}^{-1}$  are assigned to  $\text{O}=\text{C}=\text{O}$ , which is an indication of the presence of barium carbonate, a by-product of the synthesis of  $\text{BaTiO}_3$  [52]. This peak is less pronounced for the tetragonal micropowders when compared with cBT; this can indicate that the nanopowders' synthesis results in higher formation of this residual  $\text{BaCO}_3$ .

### 3.3. SEM-EDS

The SEM images in Figure 4 represent the surfaces of uncoated (A–B), Hydroxyapatite coatings produced by the HAp PS (C–F), HAp CB (G–K), HAp/cBaTiO<sub>3</sub> (L–O) and HAp/tBaTiO<sub>3</sub> (P–S), with several magnifications:  $300\times$ ,  $1000\times$ ,  $5000\times$  and  $20,000\times$ .

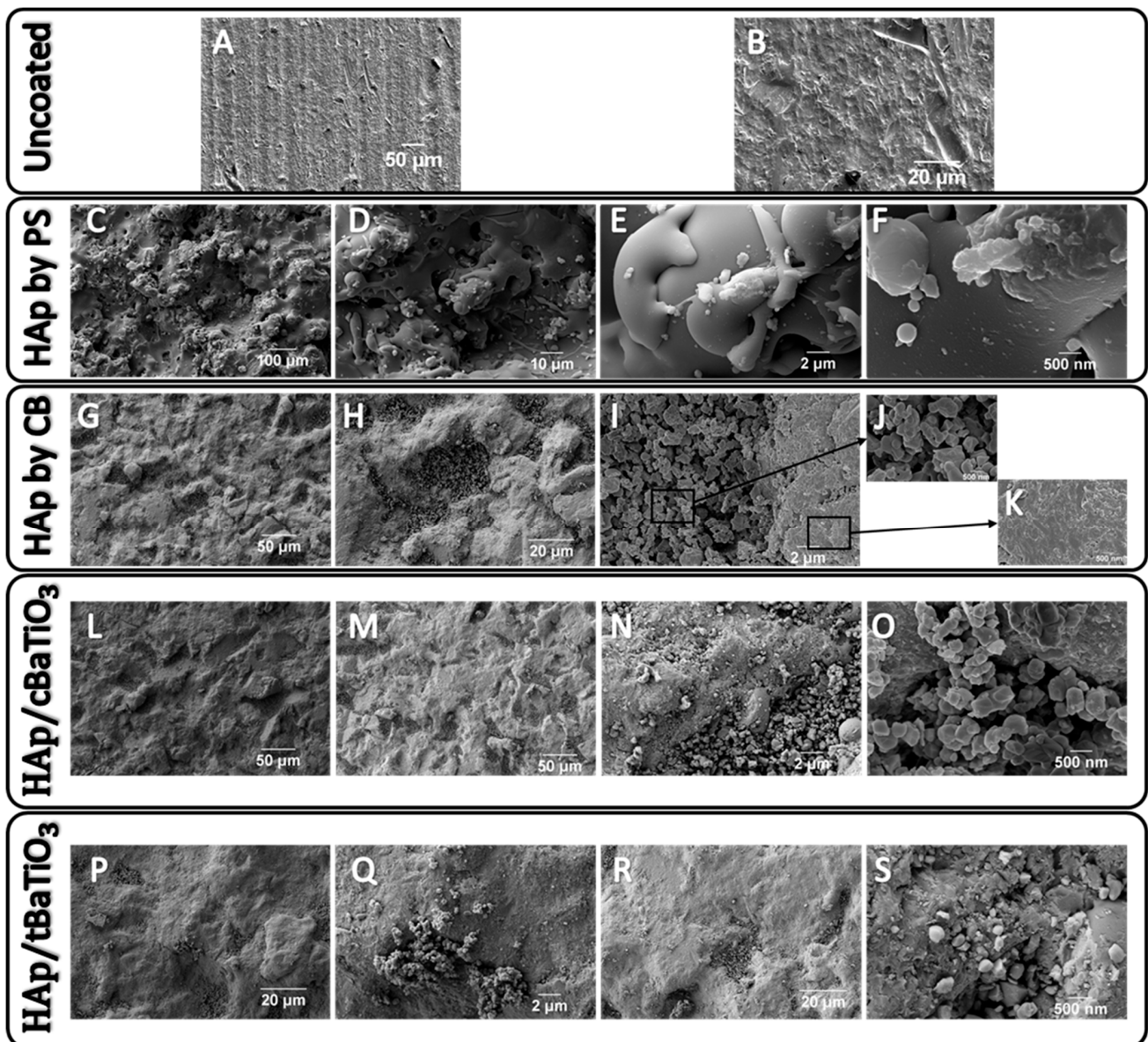


**Figure 4.** SEM images of samples without coating (A,B) and with coatings by Plasma Spray with HAp (C–F), by CoBlast<sup>TM</sup> with HAp (G–K), HAp/cBaTiO<sub>3</sub> (L–O) and HAp/tBaTiO<sub>3</sub> (P–S).

By analysing each of the uncoated substrates, it is possible to observe a regular surface with a relatively low degree of roughness, with the typical parallel lines resulting from polishing (Figure 4A,B). For the HAp coating produced by PS, the surface presented irregular morphology and roughness (Figure 4C,D) and particles deposited as droplets on the substrate, as can be seen in images E and F of the same figure. These deposited droplets are abundant and form a layer with small fragments and rounded splatters due to the plasma spray process where HAp micropowders reach the Ti-6Al-4V substrate in liquid form or in a pasty state (caused by the high temperature) so that they start to solidify in the transfer stage, and when colliding with the substrate they acquire a flat shape.

The plasma spray coatings show cracks mainly due to heat transfer from the plasma to the substrate resulting in stress gradients and thermal expansion mismatch between the substrate and the ceramic coating. When the particles solidify, a residual stress induced from rapid cooling remains [17,53]. This does not present problems for osseointegration; however, whether in vitro or in vivo, the cracks could lead to local stress concentration and induce further mechanical and physicochemical instability affecting coating adhesion [17,54].

The EDS spectra were obtained at the highlighted regions in Figure 5A and correspond to a HAp particle (Spectrum 5) and to a zone with a continuous layer of coating with small “splashes” (Spectrum 6). Spectra 5 and 6 show Ti peaks that correspond to the substrate, and the higher intensity peaks are from Ca, P and O, with a Ca/P molar ratio equal to 1.67, typical of HAp (Figure 5—Spectrum 5 and 6).

SEM images resulting from the HAp coating produced by CB show a surface with lower roughness, compared to the PS coating, as can be seen in images G and H in Figure 4. Under higher magnification, it is visible that the coating has areas with large particle agglomerates, which form a more continuous flat area and an irregular area, the latter being a result of several particles deposited on top of each other, creating voids between them since they do not fuse to form a single layer.

The EDS analysis of different regions of the sample with HAp coatings, Figure 5A,B, shows the presence of calcium, phosphorous and oxygen from hydroxyapatite ( $\text{Ca}_{10}(\text{PO}_4)_6 \cdot 2(\text{OH})$ ), titanium, aluminium and vanadium from the substrate (Ti-6Al-4V). The EDS analysis also detects Al and O, which can be attributed to the abrasive ( $\text{Al}_2\text{O}_3$ ). It is noteworthy to point out that in the XRD results (presented in Section 3.1) no other apatites were detected besides HAp.

The coatings of HAp/cBT nanopowders produced by CB are presented in images L–O in Figure 4. Surface morphology at low magnifications (L and M) is equivalent to the HAp coating produced by the same technique. However, at higher magnifications (N and O) the coating surfaces present granular deposition and poorly agglomerated particles. The particles, observed in detail in image O, can correspond to  $\text{BaTiO}_3$  nanopowders.

The last row of SEM images in Figure 4P–S present HAp/tBT micropowders in coatings produced by CB. At lower magnifications, these coatings look similar to the previous ones, namely HAp and HAp/cBT, both obtained by CB. In R and S there are still surface regions with granular deposition and poorly agglomerated particles. EDS analysis for the samples with HAp/BT, Figure 5C,D, show the same elements plus the barium from  $\text{BaTiO}_3$ .

By comparing the SEM images of different types of samples, it is possible to conclude that the ones produced by PS have a higher particle fusion compared to CB coatings, which present a granular morphology for all compositions studied.

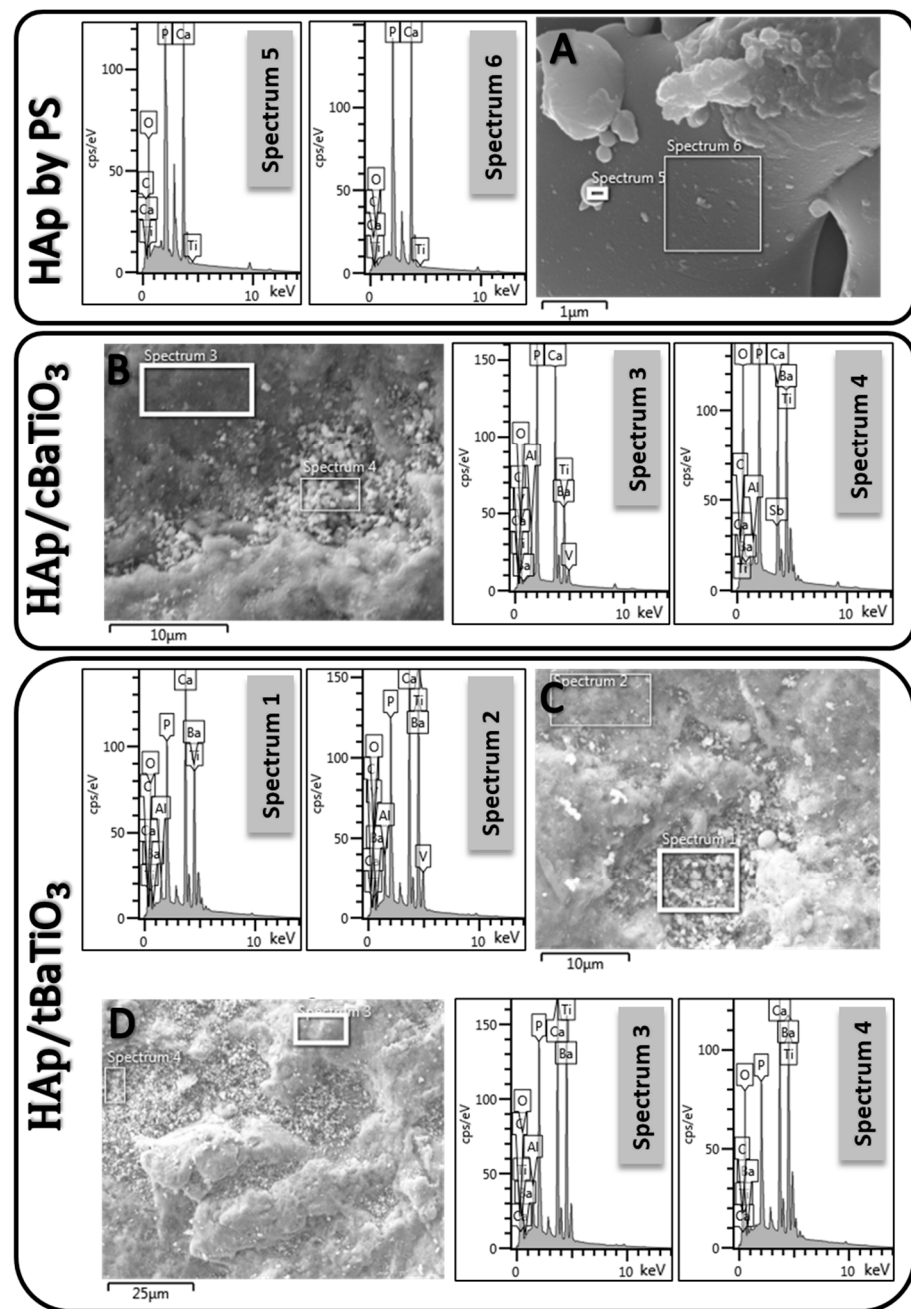


**Figure 5.** SEM/EDS images of HAp PS (A), 80%/20% (m/m) HAp/BaTiO<sub>3</sub> using BT cubic nanopowders (B) and tetragonal micropowders (C,D). The marked areas correspond to the EDS spectra shown on the same line.

### 3.4. Confocal Microscopy

Confocal microscopy was employed to achieve a 3D reconstruction of the uncoated and coated surfaces and, hence, to study the roughness at a micrometric level. The different sample images are presented in Figure 6.

Measurements made on confocal microscopy images allowed to determine the average roughness of the samples ( $W_{Sq}$ ). This property of a surface is the average depth of each point minus the mean of the data points. Additionally calculated were the skewness ( $W_{Ssk}$ ) and kurtosis ( $W_{Ssu}$ ), which are statistical parameters of the Gaussian distribution and quantify the Gaussian asymmetry and sharpness/flattening, respectively.

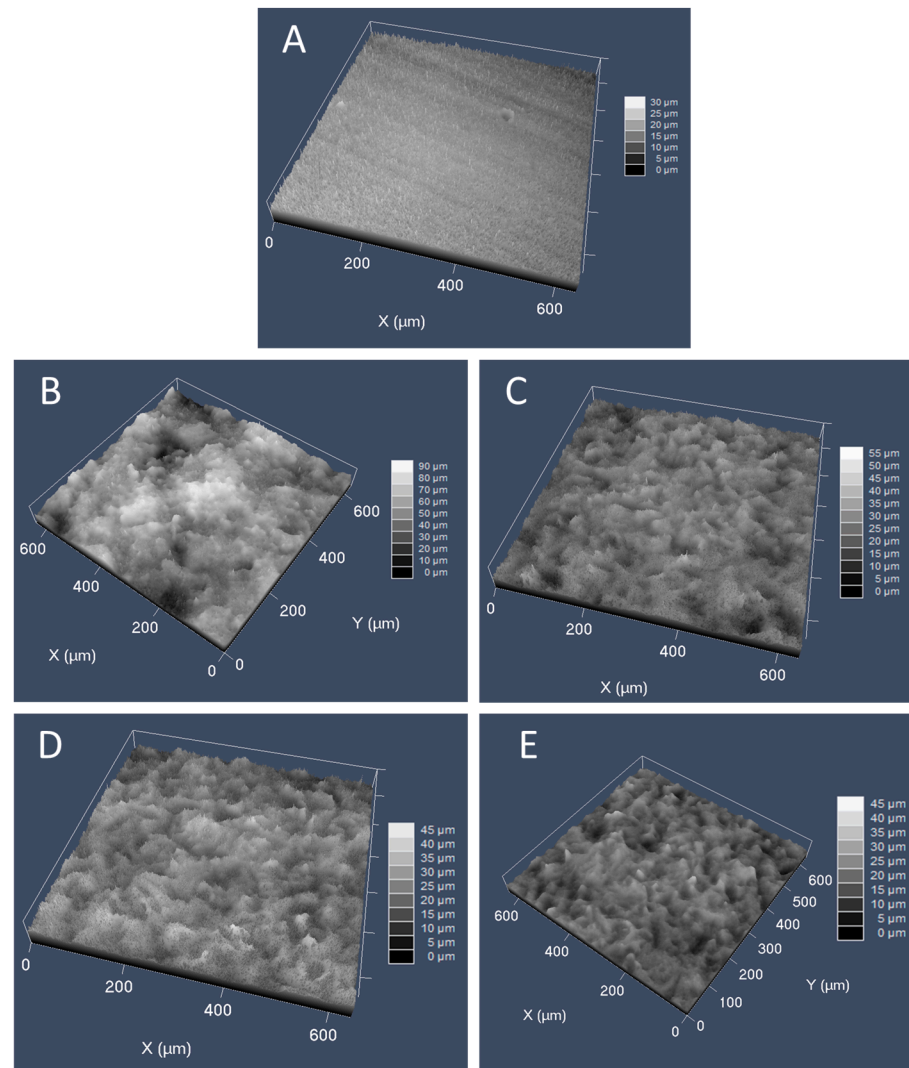


**Figure 6.** Surface topography images of Ti-6Al-4V plate (A), HAp by plasma spray coating (B) and coatings by CoBlast™ with HAp (C), 80/20 (*w/w%*) of HAp/BaTiO<sub>3</sub> with BT cubic nanopowders (D) and tetragonal micropowders (E). Images were obtained with a confocal laser microscope (the vertical scale of each of the images is set from black to white (0 to 45 μm) and the colour changes every 5 μm).

In probability and statistics, skewness and kurtosis are the third and fourth moment of the distribution (data points) [55]. The Pearson coefficients were computed; for skewness the adjusted Fisher–Pearson and for kurtosis the Pearson or excess kurtosis, respectively using Equation (4) [56], where  $N$  is the number of data points,  $x_i$  the data points and  $\bar{x}$  the mean:

$$W_{Ssk} = \frac{\sqrt{N(N-1)}}{N-2} \frac{\sum_{i=1}^N (x_i - \bar{x})^3}{\sigma^3}; W_{Ssu} = \frac{\sqrt{N(N-1)}}{N-2} \frac{\sum_{i=1}^N (x_i - \bar{x})^4}{\sigma^4} \quad (4)$$

Results are presented for all samples in Table 5. For uncoated samples and HAp coated by PS, the distribution has a negative skew, and for the remaining samples, a positive skew. Therefore, the roughness has higher values on the right side of the distribution than on the left for PS coating and the opposite happens for all CB coatings. As for the kurtosis values, all samples had a  $W_{Ssu}$  greater than 3, thus, the probability functions are leptokurtic, which means that the distributions are higher and with longer tails than the normal distribution [57].

**Table 5.** Mean roughness measurements ( $W_{Sq}$ ) of coated and uncoated samples.

| Samples                      | $W_{Sq}$ ( $\mu\text{m}$ ) | $W_{Ssk}$ | $W_{Ssu}$ |
|------------------------------|----------------------------|-----------|-----------|
| Ti-6Al-4V                    | 2.97                       | <0        | >3        |
| HAp coatings by Plasma Spray | 12.87                      | <0        | >3        |
| HAp coatings by CoBlast™     | 4.52                       | >0        | >3        |
| HAp/cBT by CoBlast™          | 4.91                       | >0        | >3        |
| HAp/tBT by CoBlast™          | 4.45                       | >0        | >3        |

According to  $W_{Sq}$  values presented in Table 5, coatings introduce a major roughness factor variation when compared to the substrates. CB coatings presented no significant change in any tested materials or the roughness, values are similar to the thickness of these coating, which is approximately 5  $\mu\text{m}$ . Comparing CB coatings with the ones produced by PS, the latter have significantly more roughness, but PS coating thickness (~13  $\mu\text{m}$ ) also has a value comparable to its  $W_{Sq}$ . The thickness of all coatings was measured immediately after deposition before the samples were removed from the CB and PS deposition setups. Qualitatively, the results found for roughness agree with the surface morphology observed in SEM images.

Considering that the presence of micro-roughness is beneficial for osseointegration, as it will facilitate cell adhesion and proliferation after implant placement [58,59], CB coating confocal results suggest that they will be able to promote cell adhesion.

### 3.5. Cytotoxicity

Cytotoxicity assays are commonly performed as the first step in the evaluation of the biocompatibility of a material. In this work, the goal is to determine if the coatings obtained by CB can be safely placed in contact with the organism. The results obtained are presented in Figure 7.

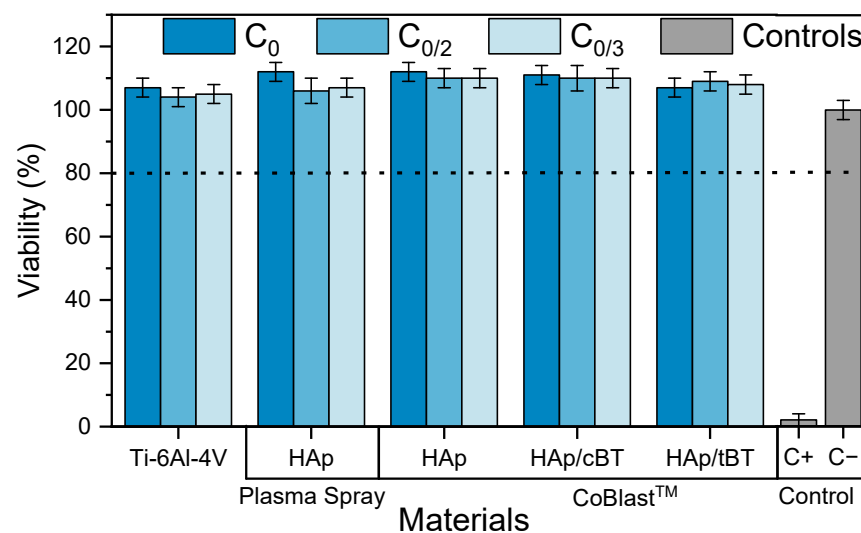


**Figure 7.** Relative cell viability in cytotoxicity tests of coated and uncoated samples.  $C_0$  is the initial concentration (0.5  $\text{cm}^2/\text{mL}$ ),  $C_{0/2}$  and  $C_{0/4}$  are dilutions by factors of two and four, C+ is the positive (cytotoxic) control and C− is the negative (nontoxic) control, both presented in gray.

The results show that for all materials, coatings and extract concentrations tested, relative cell viability is above 80%, in comparison with the negative control. These results suggest that all materials tested are biocompatible and safe to be used as coatings for implants. Moreover, these results show that the coatings under study are viable at 0.5  $\text{cm}^2/\text{mL}$ , contrary to the results presented by Ossa et al. [42]. This disparity in results should be due to the different HAp composition and not to coating process differences.

The cytotoxicity results show that the coatings produced in this work are a promising enhancement of bone prosthetics coatings, but further cell studies are recommended to confirm this hypothesis.

#### 4. Conclusions

In hydroxyapatite coatings obtained by CoBlast™, only the crystalline phase was identified, while in PS coatings of HAp, both crystalline and amorphous phases were found. For the coatings with BT obtained using CoBlast™, only the original phases of both materials were present (hydroxyapatite and barium titanate, either cubic or tetragonal). FTIR results showed that PS HAp is B-type carbonated, but for CB coatings, it was not possible to reach the same conclusion.

Regarding surface characteristics, such as homogeneity and roughness, the results show that CoBlast™ hydroxyapatite-based coatings have characteristics that promote cell adhesion. Two different composites of HAp with barium titanate were made using cubic nanopowders and tetragonal nanopowders. Results for these surfaces are similar to those obtained for coatings containing HAp only and produced by the same CoBlast™ technique. Cytotoxicity assays proved that all materials are biocompatible and suitable for biomedical applications.

In conclusion, given the properties evaluated, CoBlast™ is a viable alternative to plasma spray deposition to produce HAp-based coatings. Furthermore, the former technique has the advantage of being a room temperature process, compared to the high temperatures registered during the deposition by plasma spray.

**Author Contributions:** Conceptualization, M.C.L., J.P.M.R.B. and I.J.G.D.; methodology, M.C.L., J.P.M.R.B., E.A.P., I.J.G.D. and J.C.S.; validation, M.C.L. and J.P.M.R.B.; formal analysis, I.J.G.D., J.P.M.R.B., A.S.P., E.A.P. J.C.S. and M.C.L.; writing—original draft preparation, I.J.G.D. and A.S.P.; writing—review and editing, M.C.L., J.P.M.R.B., J.C.S.; supervision, M.C.L. and J.P.M.R.B.; funding acquisition, J.C.S., J.P.M.R.B., E.A.P. and M.C.L. All authors have read and agreed to the published version of the manuscript.

**Funding:** The authors are grateful for the FEDER funds through the COMPETE 2020 Program and National Funds through FCT—Fundação para a Ciência e a Tecnologia, I.P., in the scope of the projects LA/P/0037/2020, UIDP/50025/2020 and UIDB/50025/2020 of the Associate Laboratory Institute of Nanostructures, Nanomodelling and Nanofabrication—i3N, and DENTALBLAST project (ref. n° 17956).

**Data Availability Statement:** Data may be obtained from authors upon reasonable request.

**Acknowledgments:** The authors would like to thank M. Margarida Lima for helping with the DRX analysis.

**Conflicts of Interest:** The authors declare no conflict of interest.

#### References

1. Barrère, F.; Mahmood, T.A.; de Groot, K.; van Blitterswijk, C.A. Advanced Biomaterials for Skeletal Tissue Regeneration: Instructive and Smart Functions. *Mater. Sci. Eng. R Rep.* **2008**, *59*, 38–71. [CrossRef]
2. Bosco, R.; Van Den Beucken, J.V.; Leeuwenburgh, S.; Jansen, J. Surface Engineering for Bone Implants: A Trend from Passive to Active Surfaces. *Coatings* **2012**, *2*, 95–119. [CrossRef]
3. LaWell, C. Orthopedic Market Projected to Grow 3.4% in 2022. Available online: <https://www.orthoworld.com/orthopedic-market-projected-to-grow-3-4-in-2022/> (accessed on 18 January 2023).
4. The Orthopedic Implants Market to Be Valued at \$74.90 Billion by 2030; Expected to Witness a CAGR of 5.53%: Quintile Insights-Healthcare. Available online: <https://www.linkedin.com/pulse/orthopedic-implants-market-valued-7490-billion-2030-expected-/> (accessed on 19 January 2023).
5. Scholz, M.S.; Blanchfield, J.P.; Bloom, L.D.; Coburn, B.H.; Elkington, M.; Fuller, J.D.; Gilbert, M.E.; Muflahi, S.A.; Pernice, M.F.; Rae, S.I.; et al. The Use of Composite Materials in Modern Orthopaedic Medicine and Prosthetic Devices: A Review. *Compos. Sci. Technol.* **2011**, *71*, 1791–1803. [CrossRef]
6. Shen, P.; Chen, Y.; Luo, S.; Fan, Z.; Wang, J.; Chang, J.; Deng, J. Applications of Biomaterials for Immunosuppression in Tissue Repair and Regeneration. *Acta Biomater.* **2021**, *126*, 31–44. [CrossRef]

7. Fröhlich, L. MicroRNAs at the Interface between Osteogenesis and Angiogenesis as Targets for Bone Regeneration. *Cells* **2019**, *8*, 121. [[CrossRef](#)]
8. Jones, J.R. Scaffolds for Tissue Engineering. In *Biomaterials, Artificial Organs and Tissue Engineering*; Hench, L.L., Jones, J.R., Eds.; Woodhead Publishing: Swaston, UK, 2005; pp. 201–214. ISBN 9781855737372.
9. Hench, L.L. Biomaterials: A Forecast for the Future. *Biomaterials* **1998**, *151*, 1419–1423. [[CrossRef](#)]
10. Kato, E.; Yamada, M.; Sakurai, K. Retrospective Clinical Outcome of Nanopolymorphic Crystalline Hydroxyapatite-Coated and Anodic Oxidized Titanium Implants for 10 Years. *J. Prosthodont. Res.* **2015**, *59*, 62–70. [[CrossRef](#)]
11. Tavangar, M.; Heidari, F.; Hayati, R.; Tabatabaei, F.; Vashae, D.; Tayebi, L. Manufacturing and Characterization of Mechanical, Biological and Dielectric Properties of Hydroxyapatite-Barium Titanate Nanocomposite Scaffolds. *Ceram. Int.* **2020**, *46*, 9086–9095. [[CrossRef](#)]
12. Ielo, I.; Calabrese, G.; De Luca, G.; Conoci, S. Recent Advances in Hydroxyapatite-Based Biocomposites for Bone Tissue Regeneration in Orthopedics. *Int. J. Mol. Sci.* **2022**, *23*, 9721. [[CrossRef](#)]
13. Turner, C.H.; Burr, D.B. Basic Biomechanical Measurements of Bone: A Tutorial. *Bone* **1993**, *14*, 595–608. [[CrossRef](#)]
14. De Long, W.G.; Einhorn, T.A.; Koval, K.; McKee, M.; Smith, W.; Sanders, R.; Watson, T. Bone Grafts and Bone Graft Substitutes in Orthopaedic Trauma Surgery. A Critical Analysis. *J. Bone Jt. Surg. Am.* **2007**, *89*, 649–658. [[CrossRef](#)]
15. Santos, M.; Santos, C.; Carmezim, M.J. Production of Bioactive Hydroxyapatite Coating by Coblast Process for Orthopedic Implants. In Proceedings of the 2019 IEEE 6th Portuguese Meeting on Bioengineering (ENBENG), Lisbon, Portugal, 22–23 February 2019; pp. 1–4.
16. Prezas, P.R.; Dekhtyar, Y.; Sorokins, H.; Costa, M.M.; Soares, M.J.; Graça, M.P.F. Electrical Charging of Bioceramics by Corona Discharge. *J. Electrostat.* **2022**, *115*, 103664. [[CrossRef](#)]
17. Liu, D.M.; Chou, H.M.; Wu, J.D. Plasma-Sprayed Hydroxyapatite Coating: Effect of Different Calcium Phosphate Ceramics. *J. Mater. Sci. Mater. Med.* **1994**, *5*, 147–153. [[CrossRef](#)]
18. Landor, I.; Vavrik, P.; Sosna, A.; Jahoda, D.; Hahn, H.; Daniel, M. Hydroxyapatite Porous Coating and the Osteointegration of the Total Hip Replacement. *Arch. Orthop. Trauma Surg.* **2007**, *127*, 81–89. [[CrossRef](#)]
19. Sun, L.; Berndt, C.C.; Gross, K.A.; Kucuk, A. Material Fundamentals and Clinical Performance of Plasma-Sprayed Hydroxyapatite Coatings: A Review. *J. Biomed. Mater. Res.* **2001**, *58*, 570–592. [[CrossRef](#)] [[PubMed](#)]
20. Sun, L.; Berndt, C.C.; Grey, C.P. Phase, Structural and Microstructural Investigations of Plasma Sprayed Hydroxyapatite Coatings. *Mater. Sci. Eng. A* **2003**, *360*, 70–84. [[CrossRef](#)]
21. Xue, W.; Tao, S.; Liu, X.; Zheng, X.; Ding, C. In Vivo Evaluation of Plasma Sprayed Hydroxyapatite Coatings Having Different Crystallinity. *Biomaterials* **2004**, *25*, 415–421. [[CrossRef](#)]
22. Inadome, T.; Hayashi, K.; Nakashima, Y.; Tsumura, H.; Sugioka, Y. Comparison of Bone-implant Interface Shear Strength of Hydroxyapatite-coated and Alumina-coated Metal Implants. *J. Biomed. Mater. Res.* **1995**, *29*, 19–24. [[CrossRef](#)]
23. Dunne, C.F.; Roche, K.; Janssen, A.; Zhong, X.; Burke, M.G.; Twomey, B.; Stanton, K.T. Ultrafine Grain Formation and Coating Mechanism Arising from a Blast Coating Process: A Transmission Electron Microscopy Analysis. *Surf. Interface Anal.* **2017**, *49*, 1271–1278. [[CrossRef](#)]
24. O'Neill, L.; O'Sullivan, C.; O'Hare, P.; Sexton, L.; Keady, F.; O'Donoghue, J. Deposition of Substituted Apatites onto Titanium Surfaces Using a Novel Blasting Process. *Surf. Coat. Technol.* **2009**, *204*, 484–488. [[CrossRef](#)]
25. Barry, J.N.; Dowling, D.P. Comparison between the SBF Response of Hydroxyapatite Coatings Deposited Using Both a Plasma-Spray and a Novel Co-Incident Micro-Blasting Technique. *Key Eng. Mater.* **2011**, *493–494*, 483–488. [[CrossRef](#)]
26. Tan, F.; Naciri, M.; Dowling, D.; Al-Rubai, M. In Vitro and In Vivo Bioactivity of CoBlast Hydroxyapatite Coating and the Effect of Impaction on Its Osteoconductivity. *Biotechnol. Adv.* **2012**, *30*, 352–362. [[CrossRef](#)] [[PubMed](#)]
27. Khare, D.; Basu, B.; Dubey, A.K. Electrical Stimulation and Piezoelectric Biomaterials for Bone Tissue Engineering Applications. *Biomaterials* **2020**, *258*, 120280. [[CrossRef](#)] [[PubMed](#)]
28. Wolff, J. *The Law of Bone Remodelling*, 1st ed.; Springer: Berlin/Heidelberg, Germany, 1986; Volume 53, ISBN 978-3-642-71031-5.
29. Fukada, E.; Yasuda, I. On the Piezoelectric Effect of Bone. *J. Phys. Soc. Jpn.* **1957**, *12*, 1158–1162. [[CrossRef](#)]
30. Bodhak, S.; Bose, S.; Bandyopadhyay, A. Surface Modification and Electro-Thermal Polarisation for Bone Tissue Engineering. In *Electrically Active Materials for Medical Devices*; Imperial College Press: London, UK, 2016; pp. 103–114.
31. Gómez Batres, R.; Guzmán Escobedo, Z.S.; Carrera Gutiérrez, K.; Leal Berumen, I.; Macias, A.H.; Herrera Pérez, G.; Orozco Carmona, V.M.; Escobedo, G.; Gutiérrez, Z.S.; Leal Berumen, K.C.; et al. Impact Evaluation of High Energy Ball Milling Homogenization Process in the Phase Distribution of Hydroxyapatite-Barium Titanate Plasma Spray Biocoating. *Coatings* **2021**, *11*, 728. [[CrossRef](#)]
32. Senthilkumar, G.; Kaliaraj, G.S.; Vignesh, P.; Vishwak, R.S.; Joy, T.N.; Hemanandh, J. Hydroxyapatite—Barium/Strontium Titanate Composite Coatings for Better Mechanical, Corrosion and Biological Performance. *Mater. Today Proc.* **2021**, *44*, 3618–3621. [[CrossRef](#)]
33. Flanagan, J.; Schütze, P.; Dunne, C.; Twomey, B.; Stanton, K.T. Use of a Blast Coating Process to Promote Adhesion between Aluminium Surfaces for the Automotive Industry. *J. Adhes.* **2020**, *96*, 580–601. [[CrossRef](#)]
34. Young, R.A.; Brown, W.E. Structures of Biological Minerals. In *Biological Mineralization and Demineralization: Report of the Dahlem Workshop on Biological Mineralization and Demineralization Berlin 1981, October 18–23*; Springer: Berlin/Heidelberg, Germany, 1982; pp. 101–141. [[CrossRef](#)]

35. de Souza, C.M.P.; Militão, V.A.; Silva, I.G.; de Oliveira, R.R.; Seriacopi, V.; Junior, W.C.d.S. Characterization of Ti-6Al-4V Titanium Alloy Applied in Hydroxyapatite Coated Hip Prostheses. *Res. Soc. Dev.* **2022**, *11*, e2211830629. [CrossRef]
36. Elmer, J.W.; Palmer, T.A.; Wong, J. In Situ Observations of Phase Transitions in Ti-6Al-4V Alloy Welds Using Spatially Resolved X-ray Diffraction. *J. Appl. Phys.* **2018**, *93*, 1941. [CrossRef]
37. Selamat, M.S.; Watson, L.M.; Baker, T.N. XRD and XPS Studies on Surface MMC Layer of SiC Reinforced Ti-6Al-4V Alloy. *J. Mater. Process. Technol.* **2003**, *142*, 725–737. [CrossRef]
38. Kaschel, F.R.; Vijayaraghavan, R.K.; Shmeliov, A.; McCarthy, E.K.; Canavan, M.; McNally, P.J.; Dowling, D.P.; Nicolosi, V.; Celikin, M. Mechanism of Stress Relaxation and Phase Transformation in Additively Manufactured Ti-6Al-4V via in Situ High Temperature XRD and TEM Analyses. *Acta Mater.* **2020**, *188*, 720–732. [CrossRef]
39. Ramires, I.; Guastaldi, A.C. Study of Ti-6Al-4V Biomaterial Using Electrochemistry and XPS Techniques. *Quim. Nova* **2002**, *25*, 10–14. [CrossRef]
40. Barry, J.N.; Twomey, B.; Cowley, A.; O'Neill, L.; McNally, P.J.; Dowling, D.P. Evaluation and Comparison of Hydroxyapatite Coatings Deposited Using Both Thermal and Non-Thermal Techniques. *Surf. Coat. Technol.* **2013**, *226*, 82–91. [CrossRef]
41. Abron, A.; Hopfensperger, M.; Thompson, J.; Cooper, L.F. Evaluation of a Predictive Model for Implant Surface Topography Effects on Early Osseointegration in the Rat Tibia Model. *J. Prosthet. Dent.* **2001**, *85*, 40–46. [CrossRef] [PubMed]
42. Ossa, C.P.O.; Rogero, S.O.; Tschiptschin, A.P. Cytotoxicity Study of Plasma-Sprayed Hydroxyapatite Coating on High Nitrogen Austenitic Stainless Steels. *J. Mater. Sci. Mater. Med.* **2006**, *17*, 1095–1100. [CrossRef] [PubMed]
43. Shamray, V.F.; Sirotinkin, V.P.; Kalita, V.I.; Komlev, V.S.; Barinov, S.M.; Fedotov, A.Y.; Gordeev, A.S. Study of the Crystal Structure of Hydroxyapatite in Plasma Coating. *Surf. Coat. Technol.* **2019**, *372*, 201–208. [CrossRef]
44. Langford, J.I.; Wilson, A.J.C. IUCr Scherrer after Sixty Years: A Survey and Some New Results in the Determination of Crystallite Size. *J. Appl. Crystallogr.* **1978**, *11*, 102–113. [CrossRef]
45. Monshi, A.; Foroughi, M.R.; Monshi, M.R.; Monshi, A.; Foroughi, M.R.; Monshi, M.R. Modified Scherrer Equation to Estimate More Accurately Nano-Crystallite Size Using XRD. *World J. Nano Sci. Eng.* **2012**, *2*, 154–160. [CrossRef]
46. Demnati, I.; Grossin, D.; Marsan, O.; Bertrand, G.; Collonges, G.; Combes, C.; Parco, M.; Braceras, I.; Alexis, J.; Balcaen, Y. Comparison of Physical-Chemical and Mechanical Properties of Chlorapatite and Hydroxyapatite Plasma Sprayed Coatings. *Open Biomed. Eng. J.* **2014**, *9*, 26–39. [CrossRef]
47. Thein-Han, W.W.; Misra, R.D.K. Biomimetic Chitosan–Nanohydroxyapatite Composite Scaffolds for Bone Tissue Engineering. *Acta Biomater.* **2008**, *95*, 147–155. [CrossRef]
48. João, C.; Almeida, R.; Silva, J.; Borges, J. A Simple Sol-Gel Route to the Construction of Hydroxyapatite Inverted Colloidal Crystals for Bone Tissue Engineering. *Mater. Lett.* **2016**, *185*, 407–410. [CrossRef]
49. Franco, P.Q.; João, C.F.C.; Silva, J.C.; Borges, J.P. Electrospun Hydroxyapatite Fibers from a Simple Sol–Gel System. *Mater. Lett.* **2012**, *67*, 233–236. [CrossRef]
50. O'Sullivan, C.; O'Hare, P.; Byrne, G.; O'Neill, L.; Ryan, K.B.; Crean, A.M. A Modified Surface on Titanium Deposited by a Blasting Process. *Coatings* **2011**, *1*, 53–71. [CrossRef]
51. Mohamed, E.A.; Nabhan, E.; Ratep, A.; Hassan, F.M.; Tahoona, K. Influence of BaTiO<sub>3</sub> Nanoparticles/Clusters on the Structural and Dielectric Properties of Glasses-Nanocomposites. *Phys. B Condens. Matter.* **2020**, *589*, 412220. [CrossRef]
52. Akbas, H.Z.; Aydin, Z.; Karahan, I.H.; Dilsizoglu, T.; Turgut, S. Process Control Using FT-IR Analysis of BaTiO<sub>3</sub> from Ultrasonically Activated BaCO<sub>3</sub> and TiO<sub>2</sub>. In Proceedings of the 17th Research World International Conference, Riyadh, Saudi Arabia, 19 June 2016; Volume 11, pp. 27–30.
53. Lu, Y.P.; Li, M.S.; Li, S.T.; Wang, Z.G.; Zhu, R.F. Plasma-Sprayed Hydroxyapatite+titanium Composite Bond Coat for Hydroxyapatite Coating on Titanium Substrate. *Biomaterials* **2004**, *25*, 4393–4403. [CrossRef]
54. Radin, S.R.; Ducheyne, P. Plasma Spraying Induced Changes of Calcium Phosphate Ceramic Characteristics and the Effect on in Vitro Stability. *J. Mater. Sci. Mater. Med.* **1992**, *3*, 42. [CrossRef]
55. Siegrist, K. *Probability, Mathematical Statistics, Stochastic Processes*; LibreTexts: USA, 2023. Available online: [https://stats.libretexts.org/Bookshelves/Probability\\_Theory/Probability\\_Mathematical\\_Statistics\\_and\\_Stochastic\\_Processes\\_\(Siegrist\)](https://stats.libretexts.org/Bookshelves/Probability_Theory/Probability_Mathematical_Statistics_and_Stochastic_Processes_(Siegrist)) (accessed on 3 February 2023).
56. NIST—National Institute of Standards and Technology Measures of Skewness and Kurtosis. Available online: <https://www.itl.nist.gov/div898/handbook/eda/section3/eda35b.htm> (accessed on 2 March 2023).
57. The Complete Guide to Skewness and Kurtosis | Simplilearn. Available online: <https://www.simplilearn.com/tutorials/statistics-tutorial/skewness-and-kurtosis> (accessed on 2 February 2023).
58. Gittens, R.A.; Olivares-Navarrete, R.; Schwartz, Z.; Boyan, B.D. Implant Osseointegration and the Role of Microroughness and Nanostructures: Lessons for Spine Implants. *Acta Biomater.* **2014**, *10*, 3363–3371. [CrossRef]
59. Fukuda, N.; Kanazawa, M.; Tsuru, K.; Tsuchiya, A.; Sunarso; Toita, R.; Mori, Y.; Nakashima, Y.; Ishikawa, K. Synergistic Effect of Surface Phosphorylation and Micro-Roughness on Enhanced Osseointegration Ability of Poly(Ether Ether Ketone) in the Rabbit Tibia. *Sci. Rep.* **2018**, *8*, 16887. [CrossRef]

**Disclaimer/Publisher's Note:** The statements, opinions and data contained in all publications are solely those of the individual author(s) and contributor(s) and not of MDPI and/or the editor(s). MDPI and/or the editor(s) disclaim responsibility for any injury to people or property resulting from any ideas, methods, instructions or products referred to in the content.